SERIAL SECTIONING OF Ti-6Al-4V USING AN FIB-SEM DUAL BEAM SYSTEM

Alexander Brodsky

Submitted in Partial Fulfillment of the Requirements
for the degree of

Master of Science

Approved By:
Dr. Daniel Lewis, chair
Dr. Robert Hull
Dr. Chaitanya Ullal

Department of Materials Science and Engineering
Rensselaer Polytechnic Institute
Troy, New York

[August 2022]
Submitted August 2022

TABLE OF CONTENTS

LIST OF TABLES ..... **IV**

LIST OF FIGURES ..... **V**

ABSTRACT ..... **VI**

ACKNOWLEDGEMENT ..... **VII**

1 INTRODUCTION **1**

1.1 FOCUSED ION BEAM SERIAL SECTIONING 1
1.1.1 Overview *1*
1.1.2 Brief History *2*
1.2 ION-SOLID INTERACTIONS 4
1.2.1 Basics of Ion-Solid Interactions *4*
1.2.2 Energy Loss *7*
1.2.3 Yield *10*
1.2.4 Alloys *11*
1.2.5 Ion Channeling *12*
1.2.6 Monte Carlo Simulations *13*
1.3 ELECTRON BACKSCATTER DIFFRACTION 14
1.3.1 Coherent Scattering *15*
1.3.2 Diffuse Scattering *16*
1.3.3 Kossel Cone *17*
1.3.4 Defects *18*

2 METHODS **20**

2.1 MECHANICAL PREPARATIONS 20
2.2 ION MILLING 20
2.2.1 Chamber Geometry *21*
2.2.2 Pre-tilted Holder *23*
2.2.3 Cantilever Beam *24*
2.2.4 Beam Parameters *25*
2.3 EBSD 26

3 RESULTS **27**

3.1 NANO MILLED STRUCTURES 27
3.2 EFFECTS OF ION BEAM VOLTAGE 29
3.3 EFFECTS OF ION BEAM CURRENT 30
3.3.1 Surface features *30*
3.3.2 EBSD Results *31*

4 DISCUSSION 34

4.1 NANO-PILLAR 34
4.2 ION BEAM PARAMETERS 34
4.2.1 Ion Energy 38
4.2.2 Ion Current 39

5 CONCLUSION 40

WORKS CITED 42

APPENDICES 46

APPENDIX A ADDITIONAL NANO STRUCTURES 46
A.1 Initial nano-pillar attempt, and pattern used 46
APPENDIX B ADDITIONAL ION BEAM CURRENT IMAGES 47
B.1 SEM Images from Varied FIB Current 47
APPENDIX C ADDITIONAL EBSD IMAGES 49
C.1 FIB current effects on EBSD Overview 49

LIST OF TABLES

Table 1: Ion beam parameters 26

Table 2: Effect of FIB current, milling parameters 31

Table 3: Literature values for ion beam parameters 36

Table 4: Selected literature functional goals 37

LIST OF FIGURES

Figure 1.1: Collision cascade schematic. 4

Figure 1.2: Ion scattering and energy transfer. 7

Figure 1.3: Nuclear energy loss and reduced energy [5] 8

Figure 1.4: Preferential sputtering of a polyatomic material 11

Figure 1.5: Ion channeling 12

Figure 1.6: SRIM calculations for ion ranges [14] 13

Figure 1.7: Bragg's Law and Ewald Sphere 15

Figure 1.8: Diffusely scattered electron plume 16

Figure 1.9: Kossel Cone 17

Figure 2.1: Dual beam system chamber schematic 21

Figure 2.2: Stage maneuvers required for FIB serial sectioning 22

Figure 2.3: Cantilever beam nanostructure 24

Figure 3.1: Nano pillar 27

Figure 3.2: Nano-pillar before and after sectioning 28

Figure 3.3: Low and high energy FIB milling 29

Figure 3.4: Effect of FIB current on milled surface 30

Figure 3.5: Effect of FIB on EBSD patterns 32

Figure 3.6: EBSD patterns for FIB current of 5 nA 33

Abstract

Several experiments pertaining to optimizing focused ion beam (FIB) serial sectioning of Ti-6Al-4V were performed using FIB - SEM (scanning electron microscope) dual beam systems. The research outlined in this paper was carried out to guide efforts toward future 3D reconstructions and automated serial sectioning. The main foci of this study are the ion-solid interactions involved in FIB milling, how they could affect Electron Backscatter Diffraction (EBSD), and possible considerations and optimizations involved in performing FIB serial sectioning on Ti-6Al-4V. The results show that using a 45º pre-tilted stage holder in combination with a nano milled pillar work very well to account for the geometric constraints involved in this process. Additionally, it was found that the highest quality EBSD patterns resulted from short duration, high current, high energy ion milling of large areas. The pattern with highest band contrast was collected at the following parameters: 120 s, 5056 pA, 30 keV, 48 µm x 22 µm. This thesis should serve as a guide to those wishing to perform serial sectioning of Ti-6Al-4V and as a stepping stone for continued research into FIB serial sectioning at Rensselaer Polytechnic Institute.

ACKNOWLEDGEMENT

This work was supported by the National Science Foundation under Grant No. 1729336, "DMREF: Adaptive Control of Microstructure from the Microscale to the Macroscale".

1 INTRODUCTION

1.1 Focused Ion Beam Serial Sectioning

1.1.1 Overview

Focused ion beam (FIB) serial sectioning is a novel characterization technique for analyzing microstructural or chemical features in 3D. For polycrystalline materials, a three-dimensional analysis is highly desirable [1]. Specifically, for Ti-6Al-4V, 3D reconstructions of microstructural features could greatly contribute to current research on the material's properties and behaviors. An ongoing field of study specific to Ti-6Al-4V is its fatigue life, and the behavior and inception of fatigue cracks within the material. Ti-6Al-4V is used widely across many different industries including aerospace, automotive, medical, and consumer goods such as sports equipment. In the aerospace field, where human lives are often put at risk, it's extremely important to understand the characteristics and behavior of a part's material within its operable scope.

For example, fatigue has been found to be the most common causes of turbine-engine failure in military aircraft [2]. Better understanding of fatigue cracks, how and where they form and what their geometry is, is an ongoing field of materials science which will greatly benefit from 3D reconstructions [3]. Information on crack orientation as well as their crystallographic planes is very difficult to acquire through classical 2D characterization techniques without extrapolation. Serial sectioning facilitates accurate identification of those unique microstructural features.

In fact, most microstructural parameters, such as volumetric particle concentrations, particle or grain size distributions, grain morphology and anisotropy, and texture can only be studied as they exist, i.e. without extrapolation, with 3D reconstructions. The development of additive

manufacturing, another emerging field of materials science, depends on the analyses of those parameters; however, a large challenge posed by FIB, is the variability in microscope systems and controls as well as the variability in specimen materials and therefore the governing physics. Difficulties emerging during this research on Ti-6Al-4V as well as the lack of consistency in the literature on using FIB for this material, demonstrates the need for improving FIB serial sectioning techniques and establishing a consistent and accurate method for acquiring 3D reconstructions.

Some studies have been done which relate ion beam damage to EBSD quality [4, 5, 6, 7, 8, 9, 10] however, FIB parameters and serial sectioning methodologies, including the tedious but necessary control system improvements, are often vague or omitted from the literature leaving little chance of replication. This is usually because the optimization of beam parameters is not the focus of the studies. This thesis aims to better lay out the physics and considerations one should take to preform FIB serial sectioning of Ti-6Al-4V and facilitate and shorten the iterative experimental design process. Included among the recommended considerations are suggested ion beam parameters for sectioning Ti-6Al-4V.

1.1.2 Brief History

FIB systems were first developed at the University of Chicago and The Oregon Graduate Institute in the mid 1970s [11]. Its potential as a method of micron-scale machining was immediately realized and put into use by the semiconductor industry. In the 1980s, nano-structures were milled from integrated circuits by applying a high current density focused ion beam from a liquid metal ion source (LMIS) such as Ga. In the late eighties and early nineties, transmission electron

microscopy (TEM) foil preparation via FIB milling became widely popular, further demonstrating the use of FIB for site-specific analysis [11].

During that time, serial sectioning via cyclic mechanical grinding or polishing was being developed. In 1983, DeHoff pointed out the necessity for using serial sectioning to evaluate metallic microstructures [1]. The reason being that, although some microstructural parameters such as volume fraction or interfacial area can be obtained from classical planar analyses, or other parameters such as size distributions and anisotropy can be extrapolated from planar data, other parameters require direct 3D analysis. Such parameters include texture, distribution of triple and quadruple junctions, and general feature density per unit volume (grains, particles, defects, etc.). As material systems become more complex, with the development of superalloys and multi-layered structures, DeHoff's assertion becomes more pertinent [1].

In the late 1990s and early 2000s FIB saw its first use as a technique for producing high resolution three-dimensional maps. In 1999, Dunn and Hull presented a technique for reconstructing 3D geometry and chemical maps with lateral and depth distributions of 20 nm [12]. Up until that time, serial sectioning techniques via mechanical methods were typically very tedious and inefficient; at times taking a couple to several weeks to prepare 50 - 150 cross-sections often with a maximum depth resolution of 1 μm. In 2001, Alkemper and Voorhees developed an automated serial sectioning technique which was reported to obtain 20 sections per hour at a maximum inter-section distance of 1 μm. This method of serial sectioning does have its drawbacks, however. Besides the low depth resolution due to the distance between consecutive sections, ensuring consistency and known spacings between cross sections posed a major problem [1]. Serial sectioning this way

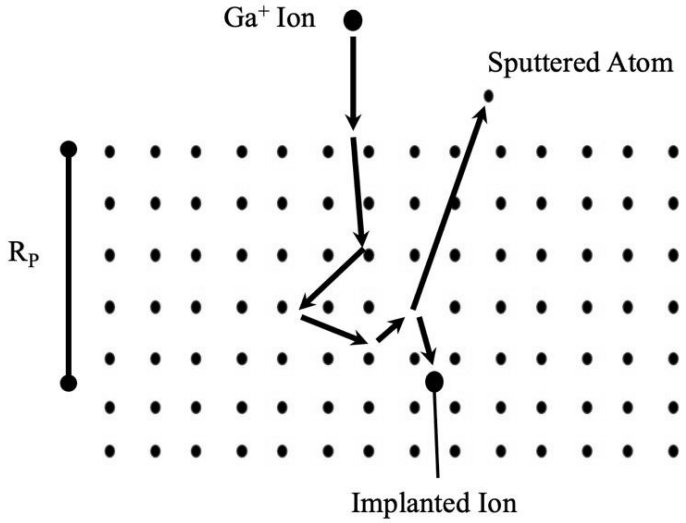

Figure 1.1: Collision cascade schematic.

As an incident ion travels through a material, it interacts with the atoms through a collision cascade. Atoms are sputtered due to the transferred energy and material can be removed for use in sectioning and micromachining.

required a complex assembly of micro-milling machines, stages, microscopes and cameras. The number of pieces of equipment required for this serial sectioning system makes it difficult to manufacture on a large scale. These issues can be mostly resolved by the FIB-scanning electron microscope (SEM) dual beam systems that were being developed at the time. In 1993, Thermo Fisher Scientific introduced one of the first commercially available dual beam systems which has led to a steady increase in publications on 3D reconstructions over the last 20 years [13].

1.2 Ion-Solid Interactions

1.2.1 Basics of Ion-Solid Interactions

The physics governing FIB milling, specifically how a material reacts when irradiated with a stream of ions, is complex. A classical mechanics model of the ion-solid interaction uses fewer parameters and simplifies the process; an incoming ion enters the target material and collides with

the atoms in a billiards-like fashion. The ion bounces around, losing energy along the way, and eventually comes to rest within the material. This process of repeated ion-atom interaction is known as a collision cascade as depicted by the schematic in figure 1.1. As the incident ion moves through the lattice, energy is transferred to the atoms, predominantly through nuclear interactions, and some atoms can be ejected and become sputtered atoms. The ion comes to rest at a distance, known as the range, below the surface and becomes an implanted ion. The range is indicated by R_P in figure 1.1 [8, 5].

R_p is the projected distance from the target material's surface to the final position of the subsurface ion. This is subtly different from other parameters such as the total distance or longitudinal distance travelled by the ion. Those distances can be measured and calculated using other models; however, the range gives a good estimate for the surface deformation layer thickness. A thicker surface deformation layer results in lower quality surface characterization data.

Typical ranges are on the order of tens of nm; for example, the range of a 5 keV Ga^+ ion impinging on Si is approximately 15 nm [5]. The energy of the incoming ion, the mass of the target atoms, and the crystal structure of the target material, as well as other factors, all change the behavior and size of the collision cascade and therefore determine the ion penetration depth. By approximating the ion-solid interaction – amorphous crystal structure, atoms behave as hard spheres, there's only on incident ion, etc. – the energy loss, dE/dx, and the range of the ion can be calculated. The energy loss due to a single atom is known as the stopping cross section of that atom, S_n [5]:

$$S_n = \frac{dE/dx}{N} \tag{1}$$

Where N is the atomic density in atoms per cm^3.

The yield is the number of sputtered atoms produced per incident ion. It strongly depends on the likelihood of a recoiled atom to overcome the surface energy barrier and escape the solid. Some significant parameters in estimating the yield of sputtered atoms are the surface binding energy, U_0, which can be estimated from the heat of sublimation (about 2 to 4 eV for most metals), the mass ratio of the ion and target atom, and the angle of incidence. Multiplying the material properties by the stopping cross section can be used to estimate the yield [5]:

$$Y \propto S_n \frac{\alpha}{U_0} \tag{2}$$

where α is a coefficient containing mass and incidence angle information. This shows that the yield is proportional to the stopping cross section and therefore also depends on the parameters listed earlier. Of these parameters, the ion energy, current, and target material can be both easily changed in modern microscope systems and have a large effect on FIB behavior. This makes them ideal input parameters for studying FIB. For instance, the Versa dual beam SEM can vary the ion accelerating voltage from 5 kV up to 30 kV and has accompanying currents ranging from as little as 10 pA to 5 nA.

The above models describe only the penetration behavior of a single ion. FIB, which relies on the collective effect of many ions, requires additional modeling. Interactions between neighboring collision cascades result in effective ranges which are statistical in nature. The probability distribution describing the ion ranges for a large population is approximately Gaussian for low implanted ion concentrations and without crystallographic channeling effects [6].

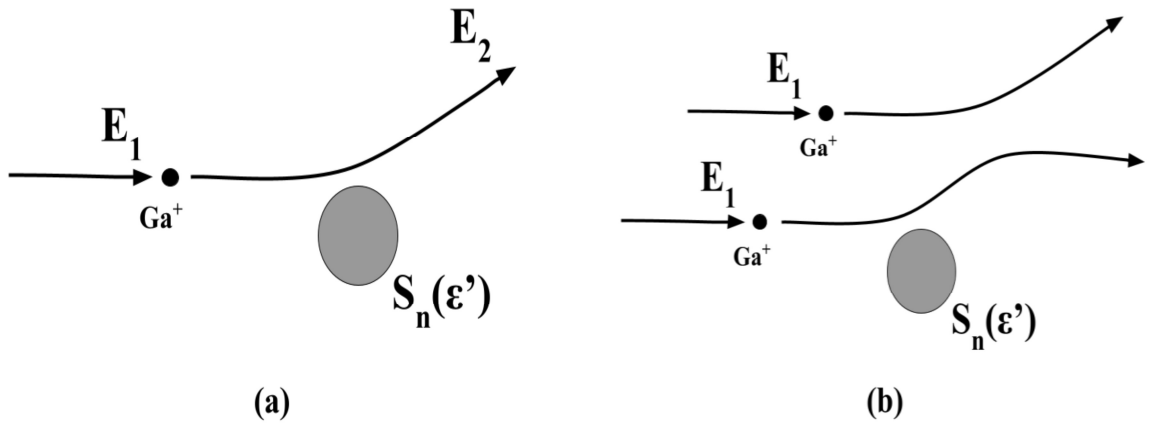

Figure 1.2: Ion scattering and energy transfer.

(a) A Ga^+ ion is deflected due to nuclear interactions (b) Ions within proximity interact with nuclei as well as with each other.

1.2.2 Energy Loss

The charged particle entering the target material will lose most of its energy through transference to either electrons (electronic energy) or nuclei (nuclear energy loss). The interaction in both cases is predominantly Coulombic; for the electronic case, the interaction potential is purely Columbic and for nuclear energy loss, the interaction potential can be modeled as a screened potential. The velocity of the particle as well as the mass of the bodies determine the extent of the interaction. Electrons, which are lighter and faster compared to the incoming ions, don't interact very strongly with the ions, and therefore have a smaller stopping cross section within the typical FIB energy ranges (5 – 30 keV). The electronic stopping cross section is largest when the ion energy is between 0.1 and 1 MeV. The relatively stationary, heavy nuclei, however, have a significant impact on the energy loss of the incoming ion. The nuclear stopping cross section peaks around 0.1 – 10 keV. Since FIB operates in the keV range, the electronic loss mechanism is insignificantly small by comparison and can therefore be ignored in estimating the total energy loss.

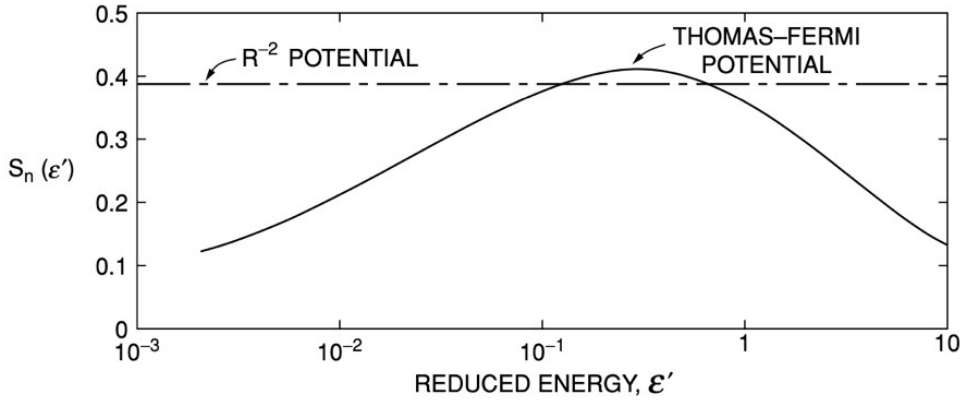

Figure 1.3: Nuclear energy loss and reduced energy [5]

The stopping cross section as a function of reduced energy for a Coulombic (R^{-2}) potential and Thomas-Fermi Potential.

The screened Coulombic potential between two atoms with atomic numbers Z_1 and Z_2 is essentially a modified Coulombic potential [5]:

$$V(r) = \frac{Z_1 Z_2 e^2 a}{2r^2} \tag{3}$$

Where *e* is the charge of an electron, *r* is the distance between the two atoms, and *a* is the screening radius for the collision with values between 0.01 – 0.02 nm for most interactions. As the ion moves past an atom, it is deflected due to the screening Coulombic potential and some energy is transferred as depicted in figure 1.2(a). The transferred energy, T, is greatest in a head-on collision and can be approximated as follows as formalized by Rutherford [5]:

$$T = \frac{4M_1 M_2}{(M_1 + M_2)^2} \tag{4}$$

where M_1 and M_2 are the masses of the two atoms. The stopping power of the atom, and therefore the energy loss, can then be calculated. Using the screened potential from (4) leads to an energy independent model for the energy loss. Alternatively, the Thomas-Fermi potential can be used to

model the interaction between the two atoms, and follows the description of Lindhard in which the nuclear energy loss is expressed in terms of a reduced energy, ϵ' [5]:

$$\epsilon' = \frac{M_2}{M_2 + M_1} E \frac{a}{Z_2 Z_2 e^2} \tag{5}$$

Figure 1.3 compares the nuclear stopping power values from the energy independent model and from the Thomas-Fermi potential. The Thomas-Fermi energy loss is [5]:

$$\frac{dE}{dx} = 4\pi a N Z_1 Z_2 e^2 \frac{M_1}{M_2 + M_1} S_n(\epsilon') \tag{6}$$

For 30 keV Ga^+ ions incident on Ti, a = 0.01nm, the reduced energy, ϵ', is 0.180 and, by using figure 1.3, the nuclear energy loss is approximately 1.1 keV/nm resulting in an approximate ion range of 27 nm.

Again, the system is being modeled as a single ion rather than a collective ensemble. The ion dose is a qualitative estimate that could be used to determine if this is a valid concern. In FIB, the dose is defined as the number of ions impinging on a given area of the target within a certain amount of time. The dose, D, in ions/cm^2 is

$$D = \frac{It}{A}(6.24 \times 10^{-17}) \tag{7}$$

where I is the current in nA (converted to ions/s by multiplying by 6.24×10^{-17}, the charge of one Ampere as well as the scale for nA and μm^2), t is the time of irradiation in seconds, and A is the area irradiated by the ions in μm^2 [8]. Typical FIB doses for micromachining nano-pillars in a reasonable amount of time, is approximately between 2 – 3 x 10^{17} ions/cm^2. This means that the average distance between the ions is about the same size as the collision cascades as shown in figure 1.2(b). Therefore, yields obtained from the results of FIB at large doses can deviate from

those calculated from the above single ion model – and pose a challenge for achieving consistent results when attempting to serial section large volumes of interest.

1.2.3 Yield

The sputtering yield, *Y*, in (2) can be expressed in a more general form as the product of two terms [5]:

$$Y = \Lambda F_d \tag{8}$$

Where Λ is a material parameter accounting for density and surface binding energies, and F_d is the deposited energy. The material parameter Λ (nm/eV) describes the energy required for an atom to overcome the surface barrier and escape the solid [5]:

$$\Lambda = \frac{4.2 \times 10^{-3}}{N U_0} \tag{9}$$

The deposited energy is the amount of energy transferred from the ion to the target material [5]:

$$F_d = cN_{\ n} \tag{10}$$

Where *c* is function of the mass ratio of the two atoms as well as the angle of incidence with values between 0.2 – 0.4. The two terms in conjunction therefore give the number of target atoms with the energy required to be sputtered by a single incident ion. (8) has the added benefit of combining all ion-material interactions into a single term. This way, experimental values for nuclear stopping powers can be estimated by measuring the atomic yield.

For 30 keV Ga+ ions normally incident on Ti, the calculated yield by using the stopping cross section estimated previously, is approximately 5.1. This is in reasonable agreement with typical measured yields of about 6 [5]. The assumption made in this approximate calculation are like those made earlier. This estimate only holds true for an ideal, amorphous, single-element material, with

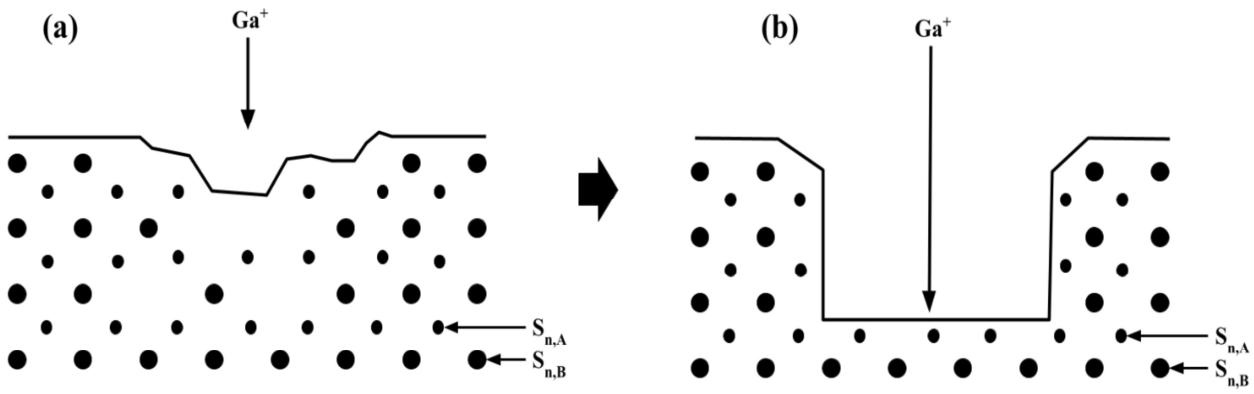

Figure 1.4: Preferential sputtering of a polyatomic material

(a) **Early sputtering of a binary alloy (b) Equilibrium sputtering of a binary alloy. The different stages produce different surfaces and can impact characterization results.**

a relatively low dose. For single-crystal, polycrystalline, or alloyed materials the above result may differ from experimental values. Additionally, highly polyatomic materials are susceptible to preferential sputtering, where, due to the differences in nuclear stopping power, the surface composition and structure will change over time. These effects are highly undesirable when attempting to quickly and accurately collect EBSD maps.

1.2.4 Alloys

Preferential sputtering is an effect which is observed when irradiating a polyatomic material, such as Ti-6Al-4V, with ions. The incident ion interacts differently with and transfers a different amount of energy to each species and the result is an inconsistent yield and variable surface composition during the transient portion of FIB sputtering. As shown in figure 1.4, during early sputtering the species with the larger stopping cross section will have a greater yield and therefore the surface composition will become less concentrated in that species. Then, as the concentration of other species are proportionally higher, the other species will have a larger yield and the system will

equilibrate. The factor f_{AB} relates the different yields due differences in surface binding energies, sputter escape depths, and energy transfers within the cascade. Measured values of f_{AB} are usually between 0.5 and 2 [5]. The steady state surface composition, $C_{A,B}(\infty)$, will then be one where the relative surface concentrations are equivalent to the bulk concentrations, $C_{A,B}{}^{b}$, scaled by the sputtering factor, f_{AB} [5]:

$$\frac{C_A(\infty)}{C_B(\infty)} = \frac{1}{f_{AB}} \frac{C_A^b}{C_B^b} \tag{11}$$

1.2.5 Ion Channeling

Ion-channeling is an effect that is observed during FIB milling of ordered materials. With ordered, crystalline materials, it is possible for the atomic planes to act as guides to carry the incoming ion in a single direction. This results in ranges that differ drastically from the earlier calculations where the solid was assumed to be amorphous [5].

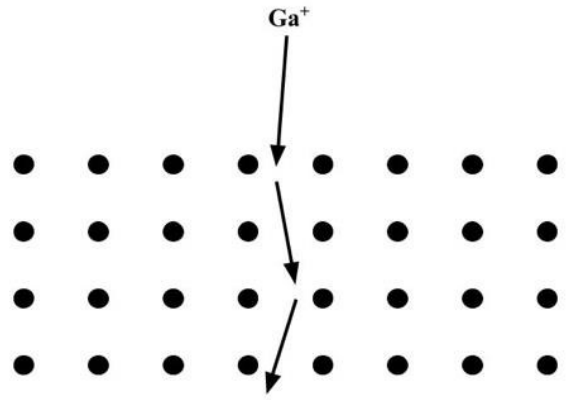

Figure 1.5: Ion channeling

A Ga^+ impinges on the sample with an energy and angle that aligns it with the crystal structure of the material. The ion is channeled through the material and can result in large implantation depths and effect EBSD characterization.

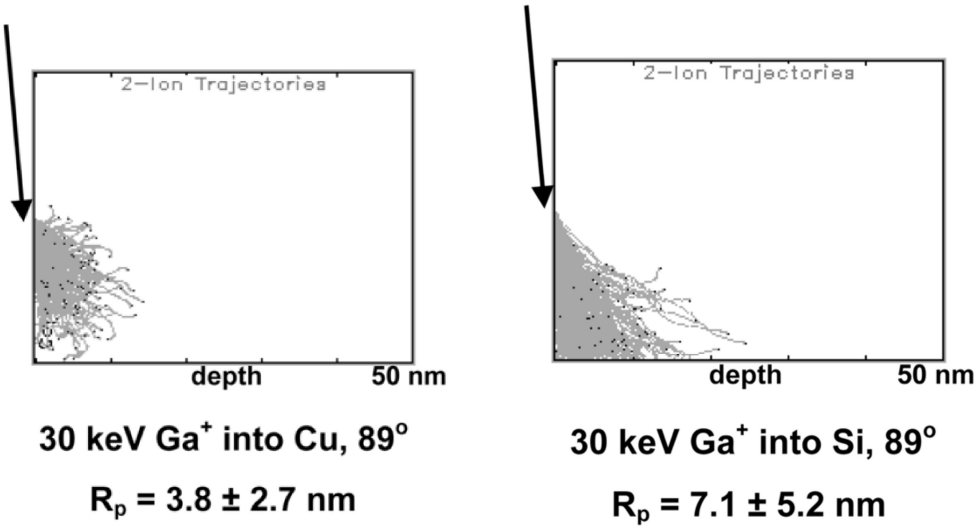

Figure 1.6: SRIM calculations for ion ranges [14]

The calculations show that the collision cascade can be a statistical process where the average range is better calculated as the mean distance travelled by the ion. With the proper model, this can be used to estimate deformation layer thickness caused by FIB.
layer thickness caused by FIB.

As shown in figure 1.5, the ion enters the material at an angle and energy that aligns with the atomic structure, and the trajectory of the ion is such that the ion glances past atoms and is steered by low-angle collisions. Although this process can be desirable for some microscopy techniques – by creating contrast from grain orientations and channeling effects – it can be justifiably undesirable for FIB milling where the ion ranges need to be minimized to not interfere with the characterization results.

1.2.6 Monte Carlo Simulations

Due to the statistical nature of a collision cascade, computational models relying on Monte Carlo simulations have been developed for calculating ion ranges. These models are beneficial for calculating statistical attributes of penetration behavior such as approximating the concentration distributions for implanted ions. The most common tool, The Stopping and Range of Ions in Matter

(SRIM) is widely used for modeling basic ion interaction volumes and penetration depths [14]. SRIM has the potential to be useful for many simple systems, especially when the experimental measurements can be difficult and potentially less accurate than interpolated data. Depending on the context, SRIM can prove to be highly applicable as an initial step; however, many assumptions are usually made to simplify and generalize the simulations. For example, a common simplification is that the structure is amorphous.

1.3 Electron Backscatter Diffraction

After FIB sputtering, the surface can then be studied through optical or electron microscopy, chemical or compositional characterizations, or structural characterizations such as electron backscatter diffraction. Since most ion beam systems come as a part of a scanning electron microscope, there is easy access to characterization techniques that rely on electron-solid interactions such as EDX or EBSD. Basic topographic and chemical information that can be acquired through SEM works well for serial sectioning of nano electronics and other multilayered structures. EBSD works well for studying alloys and microstructures. Noise in EBSD results for use with FIB serial sectioning can be caused by many factors – so understanding the underlying physics aids in understanding how to acquire clearer data. Primarily, EBSD operates on the principles of electrons interacting with single atoms and entire atomic planes. As will be seen, the structure of the atomic planes and the lack of defects within the specimen, determine the signal to noise ratio of the EBSD data.

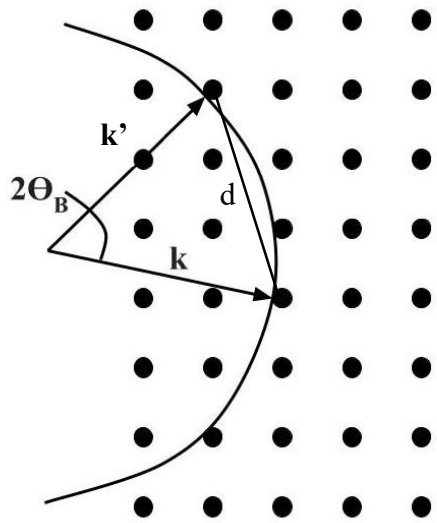

Figure 1.7: Bragg's Law and Ewald Sphere

The wave vector k in incident on the material at an angle θ_b. The angle between k and the diffracted wave, k', is therefore $2\theta_b$. At this angle, Bragg's condition is satisfied, and the waves are diffracted from planes with an interplanar spacing of d.

1.3.1 Coherent Scattering

The physics of EBSD first require modeling the incoming electrons as waves. This can be done in accordance with De Broglie and wave-particle duality. Treating the electron beam as a wave means that there will be coherent scattering from interactions with the atomic planes. This results in diffraction according to Bragg's law as seen in figure 1.7. The incoming wave, represented as the vector labeled $\boldsymbol{k}$, has a wavelength determined by the energy of the electron beam as per De Broglie's relation, higher energy results in shorter wavelengths. The incoming wave is elastically scattered by a plane of atoms, which is represented as a single point in figure 1.7, and results in the vector $\boldsymbol{k'}$. The angle between the two vectors is denoted as $2\theta_b$ which is necessarily twice the incident angle, θ_b, due to the elastic scattering of the incident wave. The circle, or sphere in 3D, which has a radius equal to the length of $\boldsymbol{k}$, is called the Ewald sphere and represents the direction and wavelength of the coherently scattered wave for every possible incident angle.

As the incident angle θ_b is changed, diffracted waves radiating from corresponding parallel atomic planes will constructively interfere. At most incident angles, the scattered waves will not be in phase with each other and there will be no peak in intensity; however, when the incident angle aligns just right with the spacing of the atomic planes, there will be constructive interference and a peak in intensity. This angle is θ_{b} and according to figure 1.7 must satisfy the Bragg equation [5]:

$$\lambda = 2dsin(\theta_b) \tag{12}$$

Here, λ is the wavelength and d is the interplanar spacing. Without coherent scattering from all parallel atomic planes, there will be added noise and reduced quality in the data. For each defect within an atomic plane, there is a correlated drop in intensity and peak broadening due to the lack in constructive interference.

1.3.2 Diffuse Scattering

When the incoming electrons enter the material, they are diffusely scattered by the atoms creating an electron plume. As shown in figure 1.8, the initially coherent electrons become incoherent

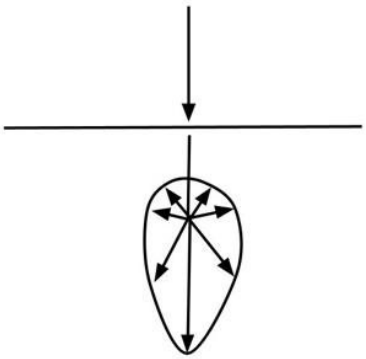

Figure 1.8: Diffusely scattered electron plume

The impinging electrons are diffusely scattered by the atoms within the material. This creates an electron plume which radiates electron waves at a range of angles and energies.

waves with a range of energies and incident angles. Bragg's law, however, still applies. This means that there will be a range of solutions and a range of intensities in three dimensions not just two dimensions as represented in figure 1.7. The three-dimensional diffraction is known as the Kossel cone and is the basis of what is seen in EBSD. [15]

1.3.3 Kossel Cone

As a result of the diffuse scattering of electrons, there will be a unique set of ***k*** vectors that satisfy Bragg's condition. Since the electrons diffuse in three dimensions, this set of ***k*** vectors is also in three dimensions as opposed to the planar example from figure 1.7. This set is known as the Kossel cone, figure 1.9, and can be thought of as Bragg's condition being revolved 360º about the mirror axis which is the axis normal to the incident plane. The descriptions of Bragg's law and the Ewald sphere can be applied as well to the Kossel cone because of their inherent relationship. Changes in the incident angle – the scattered ***k*** vector – changes the geometry of the Kossel cone and determines whether there will be an intensity peak.

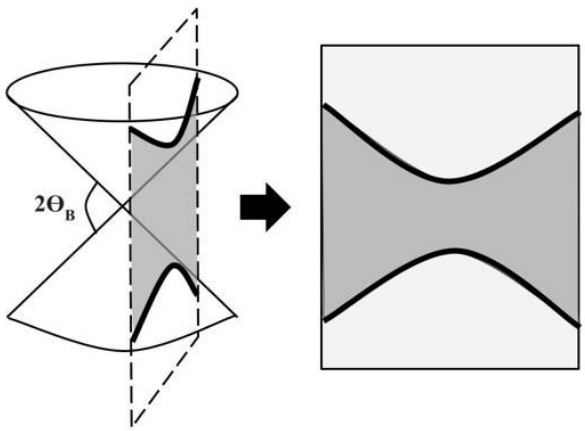

Figure 1.9: Kossel Cone

The diffusely scattered electrons result in a Kossel Cone which is diffraction in three dimensions. The Kossel cone can be captured and used for characterization with a phosphor screen.

For characterization, a phosphor screen which converts the electron intensity into light is positioned to intersect the Kossel cone as seen in figure 1.9. The resulting image from a single Kossel cone is known as a Kikuchi band and can be used to characterize different materials based on the knowledge of their atomic structure. Due to diffuse scattering of the electron, many Kossel cones land on the phosphor screen and a pattern with many Kikuchi bands is imaged. The imaged Kikuchi band, specifically its curvature and width, will change depending on the distance of the phosphor screen to the point of diffraction. Additionally, differences in lattice orientation, planar spacing, and structure alter the EBSD pattern allowing for characterization by comparing the experimental pattern with standards [15].

1.3.4 Defects

Defects in the atomic structure have a significant impact on the quality of EBSD maps. A fundamental aspect of creating peaks in intensity hinges on the existence of parallel planes scattering coherent waves that constructively interfere. An atomic plane with missing atoms or added atoms will scatter waves differently compared to a regular atomic plane. This structural difference results in a drop in overall intensity and can be a compounded effect with more defective atomic planes. Generally, defects of any nature such as local strains, due to implanted ions, vacancies, or local amorphization, will result in peak broadening and intensity and band contrast reduction for similar reasons.

In this way, EBSD is comparable to x-ray diffraction (XRD). In XRD, peak broadening can be attributed to several material abnormalities for example, nanoparticles, defects, and amorphization.

Nanoparticles result in peak broadening due to the lack of coherent scattering developing sharp peaks and defects and amorphization create peak broadening for the explanations above [16].

2 METHODS

2.1 Mechanical Preparations

Samples were prepared through a variety of methods. Samples were either cut into 15 mm thick wedges from a Ti-6Al-4V 25 mm diameter rod or cut on a bandsaw into 8 x 8 x 30mm rectangles from a 10mm thick Ti-6Al-4V sheet. The goal at this stage was to create a sample with two faces that met at approximately 90º to minimize challenges with grinding and polishing.

The samples were then mechanically ground and polished in several stages of decreasing particle size to a minimum size of 0.06 μm. Two adjacent sides were ground and polished to achieve a 90º edge between what would become the EBSD face and the sectioning face. Two faces are required to be polished since ion milling is done on two adjacent faces. The 90º angle between the two sides simplifies the geometry and facilitates the stage movements for alignments prior to milling.

2.2 Ion Milling

A VERSA 3D Dual Beam as well as a Carl Zeiss 1540EsB Crossbeam were used to preform various experiments relating to FIB serial sectioning. These included studies on the chamber-specimen-stage geometries, methods for creating a nano-pillar, and tuning of the ion beam parameters for improved EBSD data. Some aspects of the ion milling process that needed to be considered were the chamber geometries, stage maneuverability and limitations, characterization setup geometries, and the beam parameters. Controlling the FIB and its interactions with the sample are necessary to acquire maps that would be useful in a reconstruction.

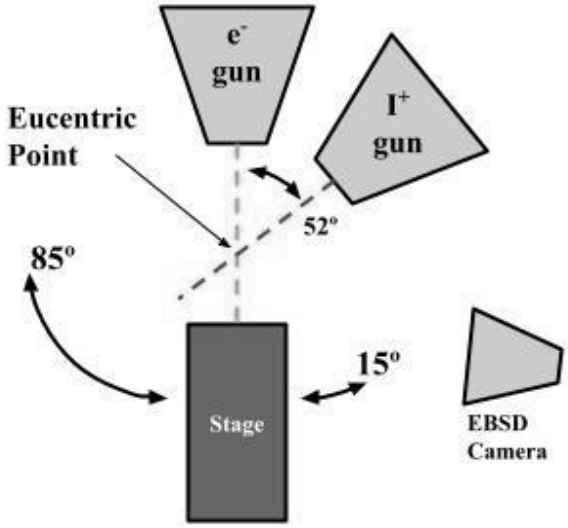

Figure 2.1: Dual beam system chamber schematic

The Versa 3D Dualbeam has the above stage range-of-motion: a maximum tilt of +85º and -15º and a possible rotation of ±180º. These limits pose a challenge for accessing all stage positions required for serial sectioning

2.2.1 Chamber Geometry

The chamber constraints of most dual beam systems – such as the location of the guns or the mechanical limitation on the stage position – necessitate several stage maneuvers between sectioning and imaging steps. The chamber schematic in figure 2.1 shows a stage capable of +85º or -15º of tilt, and ±180º of rotation. These limits constrain the stage's range-of-motion. For example, during sectioning, the surface intended for EBSD characterization is positioned parallel to the ion beam as seen in figure 2.2(c). The low incidence ion milling in this position reduces the range of the implanted ions and the thickness of the surface deformation layer. After sectioning, the sample is reoriented to preform EBSD where the same surface is angled 70º away from the electron beam as shown in figure 2.2(d). This angle is required to increase the backscatter electron yield and optimum EBSD take-off angle [15]. The difference in tilt and rotation between the two positions poses an issue. With the stage limitations shown in figure 2.1, only one of the positions

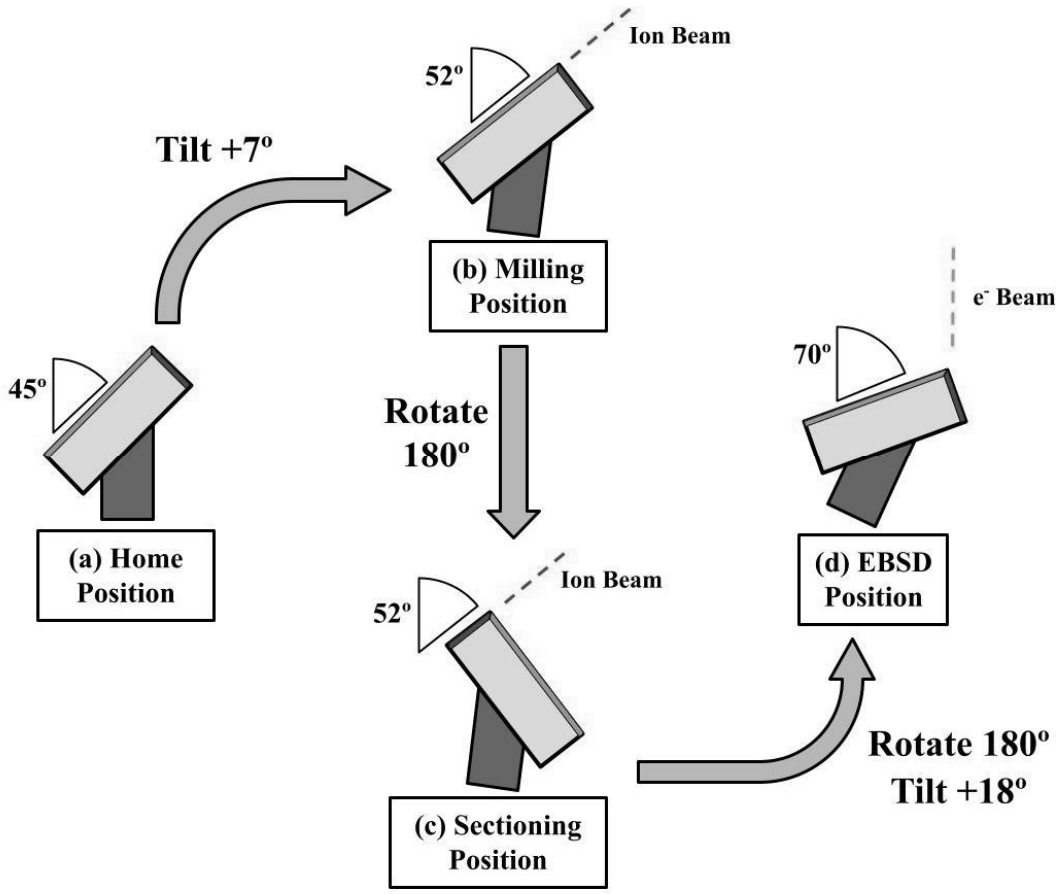

Figure 2.2: Stage maneuvers required for FIB serial sectioning

(a) the 45° pre-tilted stage in the neutral position (b) the EBSD surface (shown in red) facing the ion beam for nano-milling (c) the sectioning surface (shown in green) facing the ion beam for sectioning (d) the EBSD surface normal tilted at 70° away from the electron beam for EBSD.

is possible at a time when using a flat stage holder. If the specimen is mounted so the EBSD surface is on the side of the stage, then sectioning at 52° is possible, but EBSD is not. And if the specimen is mounted so the EBSD surface is the top surface, then EBSD at 70° is possible, but sectioning is not.

2.2.2 Pre-tilted Holder

Use of a pre-tilted holder facilitates FIB serial sectioning by avoiding issues caused by the chamber movement limitations and by reducing the total time spent repositioning sample. A pre-tilted holder pre-positions the sample more toward the center of the entire tilt range of the stage and thereby giving added range of motion for tilting in either direction. The holder can also minimize the extent of the operations – stage rotations, tilts, and pans – required between sections and therefore quickens repositioning. Just two extra minutes of repositioning between sections could potentially add hours to the total acquisition time. As shown by figure 2.2 the critical positions for serial sectioning are: (b) the EBSD surface (shown in red) facing the ion beam for nano-milling, (c), the sectioning surface (shown in green) facing the ion beam for sectioning, and, (d), the EBSD surface normal tilted at 70º away from the electron beam for EBSD. Mounting the specimen on a pre-tilted holder, such as a 45º or 38º tilt, reduces the angles through which the specimen needs to be tilted to achieve the above positions. With a 45º holder, a rotation by 180º at any tilt angle will swap the angles of the two faces. A pre-tilted holder of 32º is common for use in SEM-FIB systems that are setup according to figure 2.1. These are useful since that is the difference in angle between the sectioning position and the EBSD position – 70º - (90º - 52º) = 32º. In those cases, only a 180º rotation is needed to switch between the sectioning position and the EBSD further simplifying the process and allowing for automation. In this paper, a 45º was best since it simplifies tilt and rotation maneuvers in case the specimen edge geometry wasn't exactly 90º.

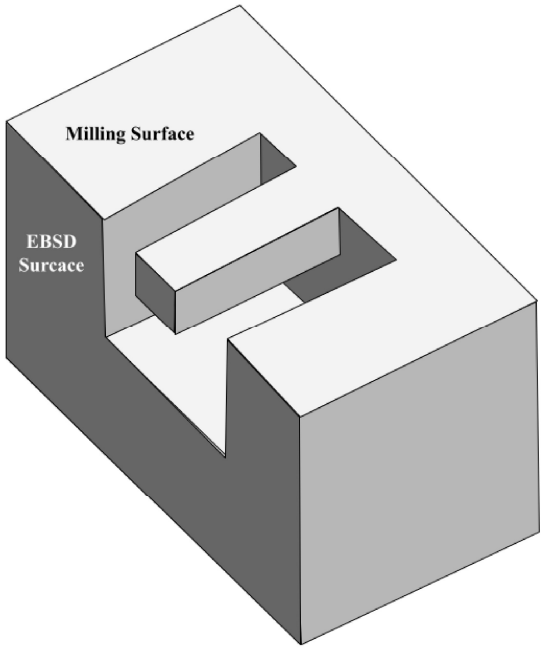

Figure 2.3: Cantilever beam nanostructure

A nanopillar containing the volume of interest is created by removing the surrounding material. During sectioning, sputtered atoms redeposit away from the EBSD surface. Additionally, shadowing during EBSD characterization is mitigated.

2.2.3 Cantilever Beam

One additional consideration on the geometry of serial sectioning is the topography changes around the volume of interest where the collision cascades are less controlled. Specifically, after several serial sections into the specimen, a ledge begins to form beneath the volume of interest. As a result, the EBSD pattern becomes obscured due to the shadowing created from the ledge. One method to circumvent this problem is by creating a cantilever beam or pillar by removing the material around the volume of interest as seen in figure 2.3. This way, serial sectioning of the volume of interest can be performed, unobstructed by its surrounding, through the entire length of the pillar.

There are multiple methods to create the nano-pillar and several additional considerations as well. Milling with the FIB always implies the risk of implantation and adding defects to the surface. For this reason, it's common to use a high energy, high current ion beam to remove as much material as possible in as little time as possible. This in known as a rough milling. Afterward, a lower energy or lower current ion beam is used as a refined milling operation to limit any possible FIB induced defects within the volume of interest. This concept of rough milling followed by a cleaning cut or refined milling is occasionally used for creating sections as well for the same reasons of defect minimization.

2.2.4 Beam Parameters

As was shown in section 1.3.4, the most important factor in preforming high quality EBSD is reducing the atomic defects and therefore controlling the interaction between the ions and the material. One challenge, however, is even minute changes to ion beam parameters can lead to drastic effects in EBSD image quality [8]. The most readily controllable parameters within an FIB system are the ion beam energy, current, and pattern (scan direction) were varied to better understand the ion beam behavior and surface topography. The first 5 rows of table 1 show the broad mix of parameters used for the initial experimentation. Due to a lack of quality EBSD patterns, a more thorough and organized optimization of the ion beam energy and current was carried out to better understand the physics within the context of sectioning Ti-6Al-4V with Ga^+ ions as seen in the final 5 rows of table 1. Noticeably, the pattern size changes somewhat between 5 keV and 30 keV as well as for low currents (1 and 3 nA) compared to high currents (5 nA). This was done to reduce the total time required for each mill since the quality of the EBSD patterns was

the focal point of these experiments – as opposed to the microstructural features, such as grains and inclusions, being imaged with EBSD which would require larger patterns.

2.3 EBSD

A range of voltages was used to produce EBSD patterns. It is generally accepted that 20 keV electrons result in the highest quality EBSD patterns. Since this study focused on the interactions between particles and matter, a range of energies from 5 keV to 20 keV was used in case there were unexpected effects arising from the electron interactions. The effect of energy on the electron beam is like its effect on the ion beam. Higher energy typically correlates to higher yields of scattered waves, and therefore sharper peaks, however, like ion interactions with materials, it's not a linear relation. There is typically a peak in the yield of scattered electron waves around 20 keV, however, this isn't always true.

Table 1: Ion beam parameters

Energy (keV)	Current (nA)	Pattern Size (μm)	Time (min.)
30	5	10 x 30 x 15	45
30	1	1.5 x 40 x 4	33
30	3	3 x 20 x 10	20
30	3	3 x 40 x 5	22
30	5	2 x 20 x 20	18
5	2.3	15 x 4 x 10	30
5	4.8	15 x 4 x 10	15
30	1	15 x 2.5 x 10	40
30	3	15 x 2.5 x 10	15
30	5	15 x 5 x 15	40

3 RESULTS

3.1 Nano Milled Structures

The nano-pillar was created by milling three trenches to form three of the four sides – the fourth side being the sectioning surface. Since the topography and defect concentration of the remaining material around the pillar wasn't of interest, a 5 nA ion beam current was used to rough mill the trenches to reduce the total milling time. The milling pattern, the scan path the ion beam would take, was important to minimize redeposition of sputtered atoms onto the pillar. Additionally, a low current around 1 nA could be used to refine the edges of the nano-pillar and to remove any possible redeposition. Since such a large volume of material is being removed while creating the nano-pillar, minimizing milling time is more important than creating a smooth surface.

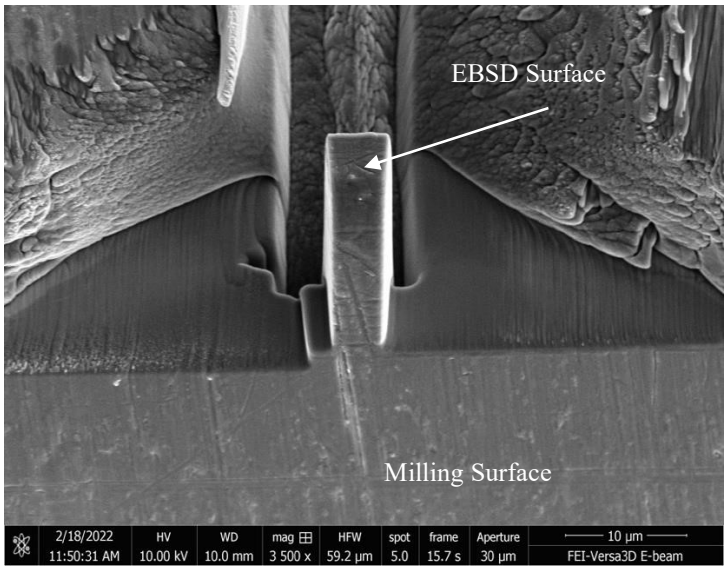

Figure 3.1: Nano pillar

A nano-pillar created by milling three trenches measuring 15 x 30 x 10 µm into the surface with a 30 keV, 5 nA ion beam. The total time was 1.5 hours. Two trenches were milled into the milling surface and one trench was milled into the EBSD surface.

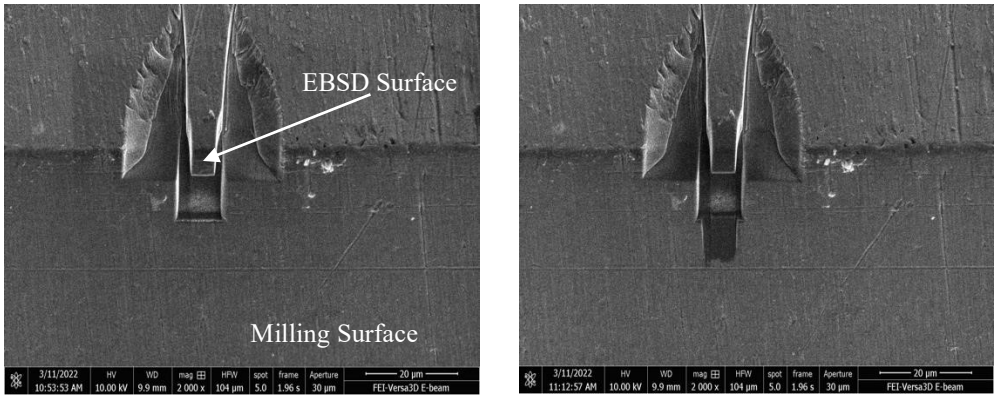

Figure 3.2: Nano-pillar before and after sectioning

A nano-pillar created by milling three trenches measuring 10 x 30 x 15 µm with a 30 keV, 5 nA ion beam. The total time was 45 minutes. The trenches were milled into the milling surface. The image on the right shows the topography after sectioning.

The pattern used to create the structure seen in the SEM image in figure 3.1 was a 'step' pattern. In this pattern, the ion beam scans a line of the desired length then slowly moves toward and with every new scan line the dwell time of the ion beam is increased. This results in a sloped trench. For figure 3.1 two trenches were milled from the sectioning position and sloped inward toward the pillar. The third trench was milled into the EBSD surface beneath the pillar. This method resulted in sharp facets of the pillar and large vacant area around the pillar.

Figure 3.2 shows a slightly different method for creating the nano-pillar. In the second method, all three patterns are milled from milling position (recall figure 2.2(b)). This resulted in a structure which was very similar to the one from the first method. A key difference between the two methods, however, is the need for additional maneuvers in the first method. The second method didn't require any repositioning of the stage to create the nano-structure which is beneficial for maintaining special accuracy and reducing milling time. Figure 3.2 also shows an SEM image of

the pillar after removing the surface layer. Additional attempts at creating the nano-pillar can be seen in appendix A.

3.2 Effects of Ion Beam Voltage

The effect of ion energy on the surface topography was also studied. With lower energy – 5keV compared to 30 keV – the stopping power is lower; however, the total initial energy is lower and therefore, overall, the implantation range is lower. With lower implantation range, there's less overall damage beneath the surface and theoretically improved EBSD pattern quality. As the stopping power is lower, the yield of atoms is also lower. Figure 3.3 shows the result of using a 5 keV ion beam (a) and using a 30 keV ion beam (b) to remove a surface layer from the EBSD face by milling into the sectioning face. The stage was in the sectioning position with the ion beam parallel to the new surface. Both beams had similar electron currents, but due to the lower energy, the 5 keV ion beam removed much less material and left behind a surface comparable in roughness to the initial surface. Visually, the higher energy ion beam seemed to establish a smooth surface

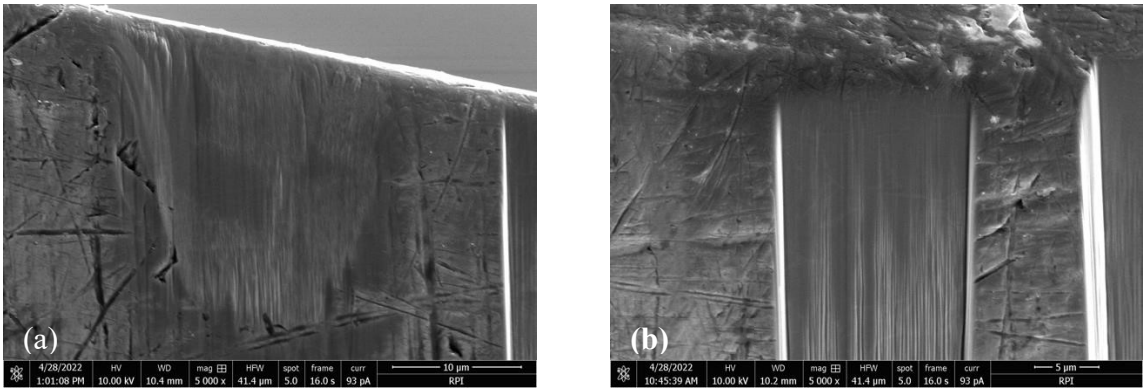

Figure 3.3: Low and high energy FIB milling

SEM images of the surface after low incidence milling with (a) a 5 keV ion beam and (b) a 30 keV ion beam.

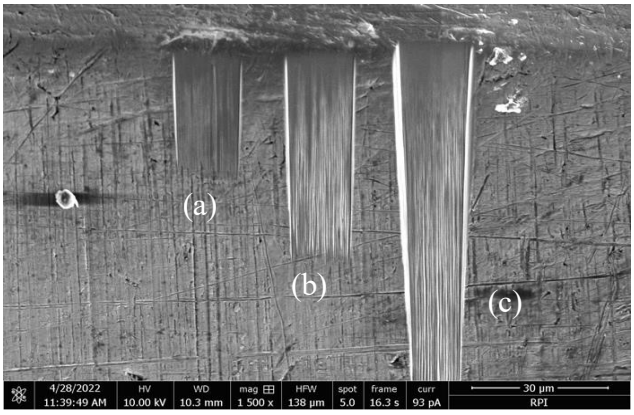

Figure 3.4: Effect of FIB current on milled surface

SEM image of three low incidence FIB mills preformed with a 30 keV ion beam at (a) 1 nA (b) 3 nA and (c) 5 nA.

after the mill. To confirm this, atomic force microscopy (AFM) for example could be used to precisely measure the roughness; although, this was not at the time.

Both surfaces exhibit curtaining which is the streaked rough face. There are several possible explanations for curtaining including surface topography, preferential sputtering, and collision cascade behavior. The curtaining effects were seen in several mills independent of ion energy, current, and time.

3.3 Effects of Ion Beam Current

3.3.1 Surface features

On a basic level of understanding, current, the number of incident ions per second, is directly related to the number of sputtered ions per second. This aspect can be seen clearly in figure 3.4. The parameters of the three mills in the figure are listed in table 2. Reduction in pattern size was done to reduce the total milling time.

Table 2: Effect of FIB current, milling parameters

Mill	Energy (keV)	Current (nA)	Pattern Size (μm)
(a)	30	1	15 x 2.5 x 10
(b)	30	3	15 x 2.5 x 10
(c)	30	5	15 x 5 x 15

Again, the mills were performed in the sectioning position with the ion beam parallel to the new surface. Also, curtaining can once again be seen in the lower portion of the mills. The curtaining seems most noticeable with the highest current, (c), and least noticeable with the lowest current, (a). Additionally, although (b) and (c) were milled with the same energy and pattern size, the depth of the cuts is very different. This is solely due to the current altering the number of sputtered atoms per second. Additional images for current controlled FIB can be seen in appendix C.

3.3.2 EBSD Results

The EBSD patterns emerging from surfaces milled from various FIB currents can be seen in figure 3.5. All mills were performed with an ion beam at 30 keV. As the current increases, it seems the band contrast and overall pattern clarity increases as well. The calculated band contrast for 50 pA was 186 and the calculated band contrast for 500 pA was 196. The calculated band contrast for 200 pA and 2 nA respectively were 216 and 204; however, these results were most likely due to the added contrast resulting from the shadowing in the bottom of the patterns. As seen in the SEM images, another aspect of high current milling is the sputter rate. When the specimen was milled with a similar time but higher current, there's more sputtering and a ledge begins to form on the bottom of the cut. This ledge creates shadowing and occludes the phosphor screen. This can be seen with the 2 nA EBSD pattern. The shadow of the ledge impaired the EBSD pattern image

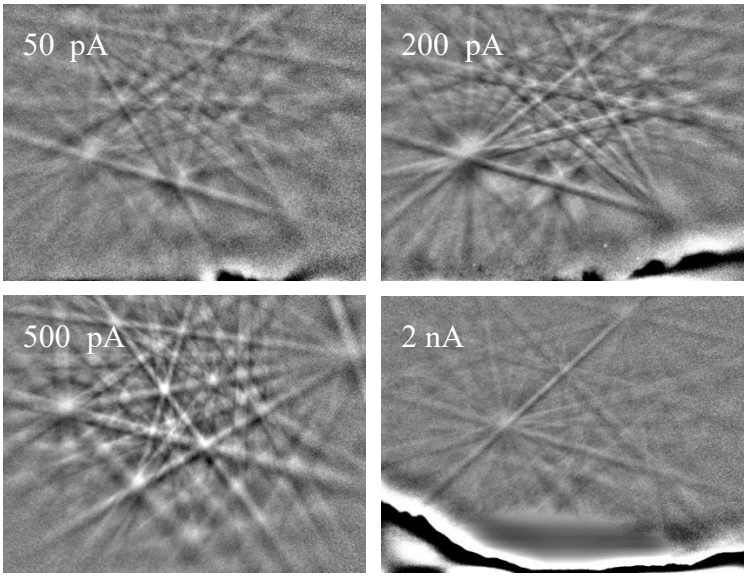

Figure 3.5: Effect of FIB on EBSD patterns

EBSD patterns of surfaces milled with a low incidence ion beam at 50, 200, 500, and 2000 pA. The shadowing at the bottom of the pattern was due to the ledge created from milling.

correction software resulting in inaccurate contrast correction for the overall pattern since the contrast was being equalized to account for the shadow.

Keeping this in mind, 5.06 nA was used to mill a new surface however, the time of the mill was very short to mitigate ledge formation. This produced the highest quality EBSD patterns, with a band contrast of 231 as seen in figure 3.6. This effected the ion dose and thereby potentially explaining the higher image quality. Additional EBSD patterns can be seen in appendix C.

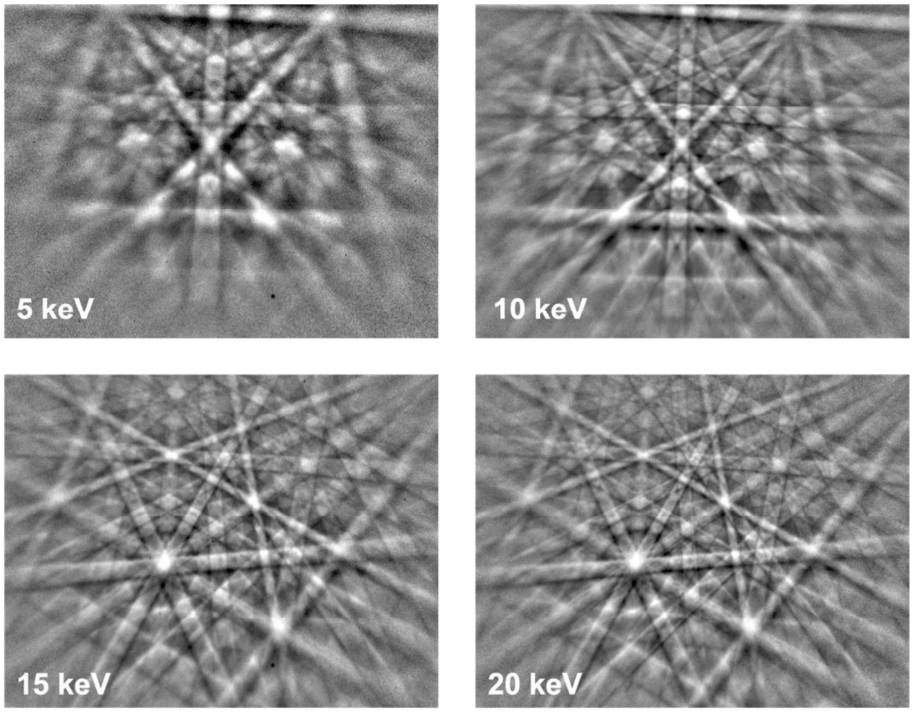

Figure 3.6: EBSD patterns for FIB current of 5 nA

EBSD patterns from a surface milled with a low incidence ion beam at 5.06 nA and an electron beam energy at 5, 10, 15, and 20 keV.

4 DISCUSSION

4.1 Nano-Pillar

The nano-pillar was ideal for controlling redeposition and EBSD occlusion. During serial sectioning, it's possible for the sputtered top surface to redeposit atop the pillar or on the new surface that will be imaged. The added room around the pillar created by the side-trenches allowed sputtered atoms to move away from the nano-pillar. Additionally, creating the sharp facets of the nano-pillar highlighted the volume of interest and would help to create well defined EBSD maps and reduce alignments errors during the reconstruction process.

The added time required for creating the nano-pillar is a valid consideration, however, the potential issues arising from undesired topography and redeposition are more important for ensuring accurate EBSD maps. Additionally, by milling all three trenches into the same surface in the milling position, the total amount of time is substantially reduced.

The size of the nano pillar should also be considered. The volume of interest is highly dependent on the context of the study, however, average grain size for Ti-6Al-4V, about 15 μm, was a good approximation for the dimensions of the nano-pillar.

4.2 Ion Beam Parameters

Before conducting investigations into the effect of FIB on EBSD patterns, a literature review was done to reduce the parameter space. It was found that the literature values usually varied widely

between papers, on similar topic even, and occasionally, parameters weren't clearly mentioned at all. The reason for this is usually due to the unique optimizations and constraints each study may face. Additionally, there are other parameters with ambiguous efficacies. Some attest to depositing a Pt layer on top of the pillar to reduce curtaining for large sections [17], however, if curtaining is due to cascade dispersion toward the bottom of the mill the Pt cap would do little to prevent this. Or some have used an alternate method of sectioning, known as rock milling, where the EBSD face is slowly rotated while the FIB beam mills parallel to the surface [18]. Supposedly this creates a smoother surface as well and improves EBSD quality.

The most direct method for optimizing the FIB process is by altering the ion beam parameters. In table 3 the literature values are described. Noticeably, the values, even those for Ti-6Al-4V span a wide range or even not mentioned (denoted with a '–') demonstrating the complex nature of FIB. Again, this is most likely a result of unique optimization processes and added adjustments for the individual microscope systems.

For this reason, the functional goals of each study are presented in table 4. The context of the serial sectioning is also highly important. As mentioned earlier, the dimensions of the volume of interest, for instance, are highly dependent on the study and can therefore vary freely. It should, however, be that current and voltage parameters are at least comparable although they could vary also depending on the study. Pilchak, for example, used an ion current of 21 nA but subsequently used a 5 keV and 1.5 nA ion beam cleaning step to improve EBSD quality. While other studies didn't use any cleaning cuts.

Table 3: Literature values for ion beam parameters

Paper	Material	Voltage (kV)	Current (nA)	Slice Thickness (μm)	Area (μm)
Mateescu 2007	FCC: Al,Cu,Au	30	2	0.2	25x7
Konrad 2006	Fe Alloy	30	0.5	2	20x50
Xu 2006	Fe, Ni	30	3	0.5	20x20
Zaefferer 2008	FeC0.49	30	-	0.1	30x20
Groeber 2006	IN100	-	3	0.25	40x41
Uchic 2007	IN100	30	3	0.25	41x41
Uchic 2006	IN100	-	3	0.125	48x47
Matteson 2001	Si	5	0.06	-	-
He 2012	TA15	30	0.5	0.2	30 x 20
Ding 2010	Ti	30	0.3	0.15	-
Tiley 2014	Ti	30	6.5	-	-
Everaerts 2017	Ti-6Al-4V	30	20	-	-
Jha 2011	Ti-6Al-4V	30	6.5	-	75x50
Pilchak 2009	Ti-6Al-4V	30	21	-	-
DeMott 2021	Ti-6Al-4V, AM	-	-	0.1	40x40
Dillon 2009	Y	30	7	0.28	30x40

Table 4: Selected literature functional goals

Paper	Goals
Alkemper 2001 [1]	Present a novel method for mechanical serial sectioning via automated mechanical micro milling
DeMott 2021 [17]	Methods and algorithms for characterizing Ti microstructural features acquired from Plasma FIB Serial Sectioning
Dillon 2009 [19]	Determine Y grain-boundary character distributions and energies from 3D reconstructions using FIB
Ding 2010 [7]	Analyze hydride formation in Ti thin films and the effect of FIB milling on precipitation of hydride
Everaerts 2017 [3]	Analyze Ti fatigue crack initiation facets using FIB and EBSD
Groeber 2006 [20]	Characterize and compile 2D sections taken from FIB-EBSD sectioning for improved reconstructions
He 2012 [21]	Study 3D morphology and crystal orientation distributions of a Ti allow using dual beam serial sectioning
Hull 1999 [12]	Present a novel technique for creating high lateral resolution chemical and geometric 3D Reconstructions using FIB
Inkson 2000 [22]	Study subsurface nanoindentation via 3D reconstructions of sequential 2D maps acquired by FIB
Jha 2011 [23]	Characterize fatigue crack initiation facets in Ti using FIB-EBSD serial sectioning
Jones 2016 [8]	Investigate phase transformation in Co induced by FIB at a range of doses and incident angles
Konrad 2006 [24]	3D EBSD-FIB reconstruction to study orientation gradients around a hard Laves particle in a Fe alloy
Li 2009 [25]	3D EBSD-FIB reconstruction to study relative grain boundary area and energy distributions in Ni
Mateescu 2007 [26]	Study the effect of Ga+ FIB on EBSD pattern quality of FCC metals
Matteson 2001 [14]	Correlate FIB induced damage in Si and Cu for a range of energies and incident angles with EBSD pattern quality
Michael 2011 [4]	Correlate FIB dose with microstructural changes in Cu, Au, and W including texture development, grain growth, and intermetallic formation
Pilchak 2009 [27]	3D EBSD-FIB reconstruction for analysis of Ti fatigue crack initiation and growth
Tiley 2014 [18]	Characterize stir welded Ti microstructure using 3D EBSD-FIB reconstructions
Uchic 2007 [28]	Review developments and applications of FIB for use in creating 3D reconstructions
Uchic 2006 [29]	Demonstrate the capabilities of 3D EBSD-FIB reconstructions through the characterization of Ni superalloys
Volkert 2007 [30]	Review basics of ion-solid interactions and applications of FIB microscopy and micromachining
Wirth 2008 [11]	Demonstrate the ability of FIB combined SEM or TEM to study geomaterials on a nanometer scale
Xu 2006 [9]	Review techniques for generating 3D EBSD microstructures by FIB tomography
Zaefferer 2008 [10]	Present progress made toward automating and optimizing 3D orientation microscopy in a dual FIB–SEM system

4.2.1 Ion Energy

The results showed a difference in surface topography between the 30 keV and 5 keV ion beam. With the higher ion energy, more material is removed in the same amount of time so less total time, and ion dose, is required for sectioning. Whereas the 5 keV ion beam removes less material, it also creates a thinner defective layer within the material which is better for EBSD. It is possible that combining an initial 30 keV cut followed by a 5 keV cleaning mill could produce even better EBSD patterns; however, the added time, and challenges that come with operating an FIB at low energy mostly negates the need for a cleaning step if high quality patterns are accessible with just 30 keV ions.

Furthermore, some FIB-SEM dual beam systems such as the Zeiss Crossbeam, either don't have access to low energy ion beams or the alignment systems, which may require tedious mechanical tuning and beam focusing, make low energy ion beam milling inconsistent or unnecessarily complicated. Therefore, a 5 keV cleaning step is most likely unnecessary for serial sectioning of Ti-6Al-4V.

The penetration depth and amorphous layer thickness is a concern of 30 keV ions. For milling Ti-6Al-4V the penetration depth of 30 keV Ga^+ is roughly 27 nm. For EBSD with 20 keV electrons, the depth sensitivity, calculated from electron escape depth, is between 10 – 40 nm. This comparison is key for determining whether a lower energy cleaning cross section is necessary. By comparison, the range for 30 keV Ga^+ in Si is about 63 nm and the amorphization layer thickness and EBSD quality reduction is a known issue with serial sectioning of Si.

4.2.2 Ion Current

The effect of ion current on the specimen topography and resultant EBSD patterns can be very complicated. For basic calculations, it is often assumed that the ion current has no effect on sputtering; however, it would make sense that if the beam current, specifically the ion flux through a certain beam width, was high enough, the ion-ion interactions would create deviations from the calculations. A similar attribute to the beam current, and one that expresses the ion density, is the ion dose. It's been shown that the ion dose does significantly alter the ion beam behavior [4] [8]. For this reason, the ion current effects were investigated.

The results showed that the ion current, and the dose, does affect the quality of the EBSD images. Specifically, the highest quality EBSD images were acquired using a 5.65 keV ion beam for only 120 seconds on a large area. This results in a relatively low ion dose and therefore a low ion concentration.

5 CONCLUSION

Serial sectioning with FIB is a highly important and emerging field within material science characterization. The ability to understand microstructural features in 3D is extremely pertinent for many fields of research where classical 2D characterization and microscopy techniques don't suffice. For example, fatigue behavior and fatigue crack formation, by nature, require an understanding in three dimensions. Additionally, grain distributions and morphologies are inherently 3D and therefore require a 3D analysis. The modern technique for creating 3D reconstructions by FIB serial sectioning hinges on understanding and controlling the ion interactions within the specimen. The fundamentals of ion-solid interactions are nuclear energy loss and collision cascades. The phenomena that arise due to focused ion beam milling are atomic sputtering, preferential sputtering, and ion channeling. EBSD is also a requirement for serial sectioning with FIB. The principles of FIB consist of crystallographic planes coherently scattering electron waves creating intensity peaks. For this reason, an order structure with minimal defects is needed for high quality EBSD patterns.

For performing FIB serial sectioning on Ti-6Al-4V with the VERSA 3D Dual Beam, a 45º pre-tilted holder was used. The pre-tilted holder greatly facilitated milling operations by reducing and simplifying the necessary stage maneuvers. Additionally, a high current ion beam was used to mill a nano-pillar. The nano-pillar prevented EBSD occlusion as well as redeposition.

The ion beam voltage and current effects on the topography and resultant EBSD quality was studied. The ion voltage correlated mostly with the sputter yield, however, it also correlated with

the ion implantation range. It was found that low energy ion milling adds unnecessary complications for FIB serial sectioning of Ti-6Al-4V. The ion current effects the sputter yield as well as the collision cascade behavior. There appeared to be a correlation between current and surface roughness however, it was clear that further analysis with AFM or other techniques were needed. A more erratic collision cascade may have resulted in rougher surfaces, however, by reducing the milling time, and therefore the dose, the surface was optimized for EBSD sheerly according to the EBSD band contrast values. The highest quality EBSD pattern was attained by using an ion beam with the following parameters: 30 keV, 5650 pA, 120 seconds total milling time.

With the information provided in this thesis, the next steps would be toward acquiring complete 3D reconstructions of Ti-6Al-4V. This can be done by combining the research on the nanopillar geometry with the optimized ion beam sectioning parameters to achieve several consecutive EBSD maps. Further work would include metrological investigations to improve lateral resolution and ease of map alignment in creating reconstructions. Additionally, machine code scripts can be developed to automate serial sectioning. Alternatively, Zaefferer et al. have developed automated serial sectioning algorithms for other materials [10]. It would also be possible to take the information from this thesis and investigate beam optimizations for other materials.

WORKS CITED

[1] J. Alkemper, "Quantitative serial sectioning analysis," *Journal of Microscopy,* vol. 201, no. 3, pp. 388-394, 2001.

[2] R. Nalla, "On the influence of mechanical surface treatments deep rolling and laser shock peening on the fatigue behavior of Ti-6Al-4V at ambient and elevated temperatures," *Materials Science and Engineering,* vol. 355, no. A, pp. 216-230, 2003.

[3] J. Everaerts, "Investigation of fatigue crack initiation facets in Ti-6Al-4V using focused ion beam milling and electron backscatter diffraction," *Journal of Microscopy,* vol. 267, no. 1, pp. 57-69, 2017.

[4] J. R. Michael, "Focused Ion Beam Induced Microstructural Alterations: Texture Development, Grain Growth, and Intermetallic Formation," *Microsc. Microanal.,* vol. 17, pp. 386-397, 2011.

[5] T. L. Alford, L. C. Feldman and J. W. Mayer, Fundumentals of Nanocale Film Analysis, New York: Springer, 2007.

[6] L. A. Giannuzzi, "Ion-Solid Interactions," in *Introduction to Focused Ion Beams*, New York, Springer, 2005, pp. 13-52.

[7] R. Ding, "In situ hydride formation in titanium during focused ion milling," *J. of Electron Microscopy,* vol. 60, no. 1, pp. 1-9, 2011.

[8] H. Jones, " Electron backscatter diffraction studies of focused ion beam induced phase transformation in cobalt," *Materials Characterization,* vol. 120, pp. 210-219, 2016.

[9] W. Xu, "Techniques for generating 3-D EBSD microstructures by FIB tomography," *Materials Characterization,* vol. 58, pp. 961-967, 2007.

[10] S. Zaefferer, "Three-Dimensional Orientation Microscopy in a Focused Ion Beam–Scanning Electron Microscope: A New Dimension of Microstructure Characterization," *Met. and Mat. Trans.,* vol. 39, no. A, pp. 374-389, 2008.

[11] R. Wirth, "Focused Ion Beam (FIB) combined with SEM and TEM: Advanced analytical tools for studies of chemical composition, microstructure and crystal structure in geomaterials on a nanometre scale," *Chemical Geology,* vol. 261, pp. 217-229, 2009.

[12] R. Hull and D. Dunn, "Reconstruction of three-dimensional chemistry and geometry using focused ion beam microscopy," *Appl. Phys. Lett.,* vol. 75, no. 21, pp. 3414-3416, 1999.

[13] J. Williams, "The Dual-Beam—Its Birth, Progress, and Future.," *Microscopy Today,* vol. 22, no. 4, pp. 32-37, 2014.

[14] T. Matteson, "Electron Backscattering Diffraction Investigation of Focused Ion Beam Surfaces," *J. of Electronic Materials,* vol. 31, no. 1, pp. 33-39, 2002.

[15] A. J. Schwartz, Electron Backscatter Diffraction in Material Science, New York: Springer, 2009.

[16] P. Muhammed Shafi, "Impact of crystalline defects and size on X-ray line broadening: A phenomenological approach for tetragonal SnO2 nanocrystals," *AIP Advances,* vol. 5, no. 057137, pp. 1-10, 2015.

[17] R. Demott, "3D electron backscatter diffraction characterization of fine α titanium microstructures: collection, reconstruction, and analysis methods," *Ultramicroscopy,* vol. 230, no. 113394, 2021.

[18] J. Tiley, "3D reconstruction of prior β grains in friction stir–processed Ti–6Al–4V," *J. of Microscopy,* vol. 255, no. 2, pp. 71-77, 2014.

[19] S. J. Dillon, "Characterization of the Grain-Boundary Character and Energy Distributions of Yttria Using Automated Serial Sectioning and EBSD in the FIB," *J. Am. Ceram. Soc,* vol. 92, no. 7, pp. 1580-1585, 2009.

[20] M. Groeber, "3D reconstruction and characterization of polycrystalline microstructures using a FIB–SEM system," *Materials Characterization,* vol. 57, pp. 259-273, 2006.

[21] D. He, "Three-Dimensional Morphological and Crystallographic Investigation of Lamellar Alpha and Retained Beta in a Near Alpha Titanium Alloy by Combination of Focused Ion Beam and Electron Backscattering Diffraction," *Steel Research Int.,* vol. 83, no. 5, pp. 496-500, 2012.

[22] B. Inkson, "Subsurface nanoindentation deformation of Cu±Al multilayers mapped in 3D by focused ion beam microscopy," *J. of Microscopy,* vol. 201, no. 2, pp. 256-269, 2001.

[23] S. K. Jha, "Characterization of fatigue crack-initiation facets in relation to lifetime variability in Ti–6Al–4V," *Int. J. of Fatigue,* vol. 42, pp. 248-257, 2012.

[24] J. Konrad, "Investigation of orientation gradients around a hard Laves particle in a warm-rolled Fe3Al-based alloy using a 3D EBSD-FIB technique," *Acta Materialia,* vol. 54, pp. 1369-1380, 2006.

[25] J. Li, "Relative grain boundary area and energy distributions in nickel," *Acta Materialia,* vol. 57, pp. 4304-4311, 2009.

[26] N. Mateescu, "Some factors affecting EBSD pattern quality of Ga+ ion-milled face centred cubic metal surfaces," *Materials Chemistry and Physics,* vol. 106, pp. 142-148, 2007.

[27] A. Pilchak, "Crystallography of Fatigue Crack Initiation and Growth in Fully Lamellar Ti-6Al-4V," *Met. and Mat. Trans.,* vol. 41, no. A, pp. 106-124, 2010.

[28] M. D. Uchic, "3D microstructural characterization of nickel superalloys via serial-sectioning using a dual beam FIB-SEM," *Scripta Materialia,* vol. 55, pp. 23-28, 2006.

[29] M. D. Uchic, "Three-Dimensional Microstructural Characterization Using Focused Ion Beam Tomography," *MRS Bulletin,* vol. 32, pp. 408-416, 2007.

[30] C. Volkert, "Focused Ion Beam Microscopy and Micromachining," *MRS Bulletin,* vol. 32, pp. 389-399, 2007.

APPENDICES

Appendix A Additional Nano Structures

A.1 Initial nano-pillar attempt, and pattern used

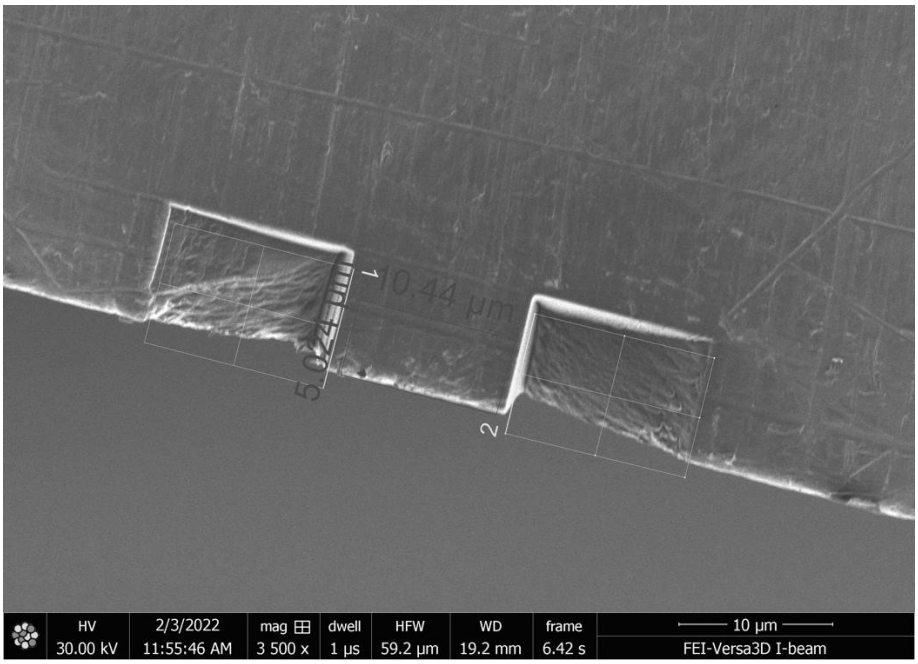

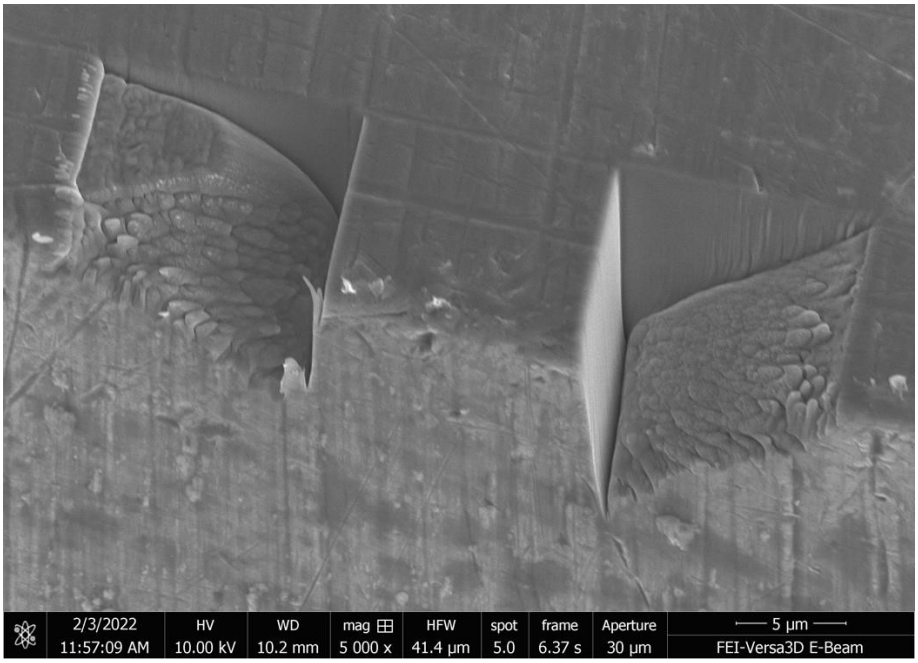

Appendix B Additional Ion Beam Current Images

B.1 SEM Images from Varied FIB Current

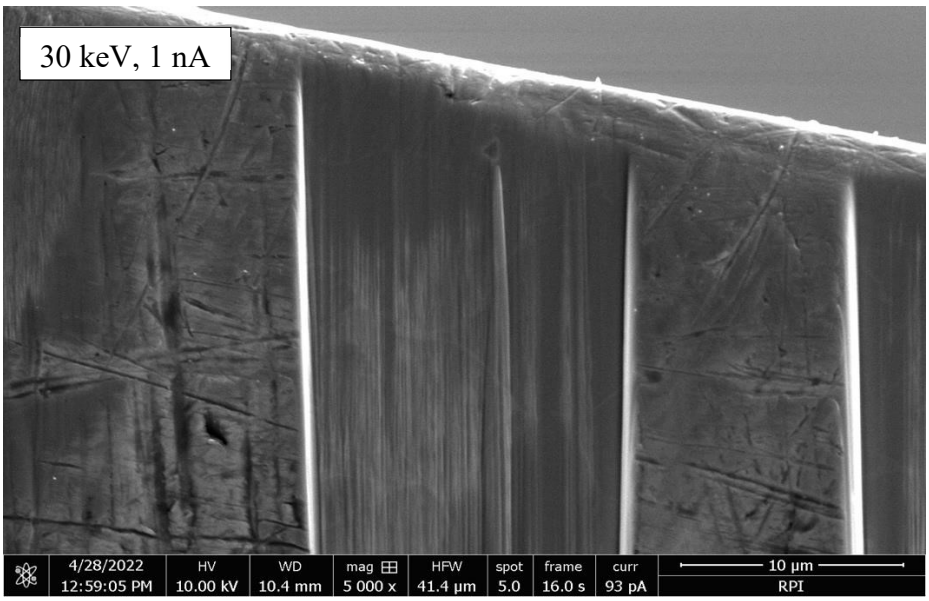

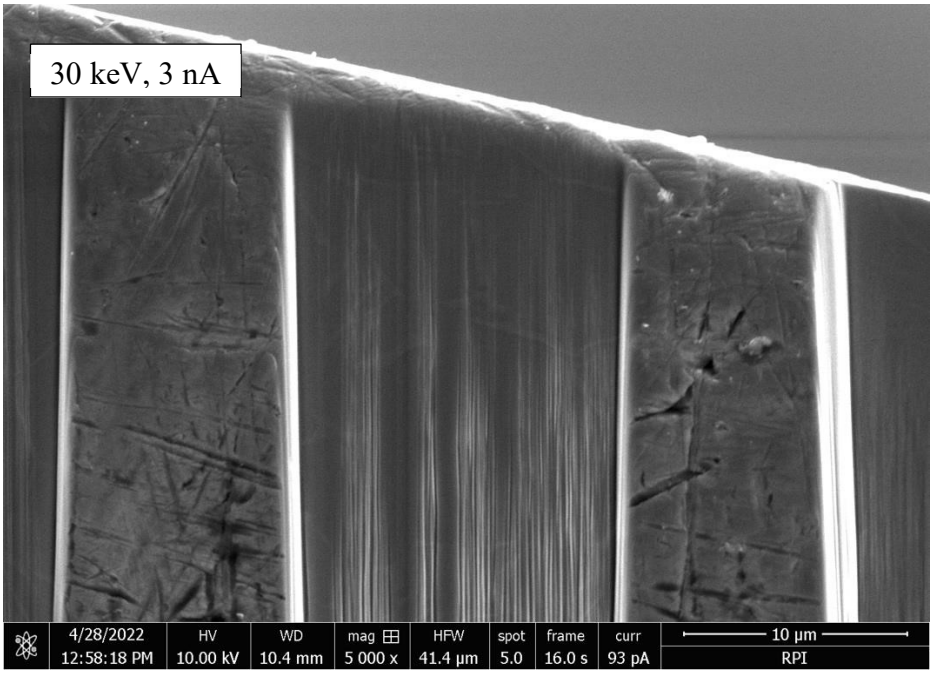

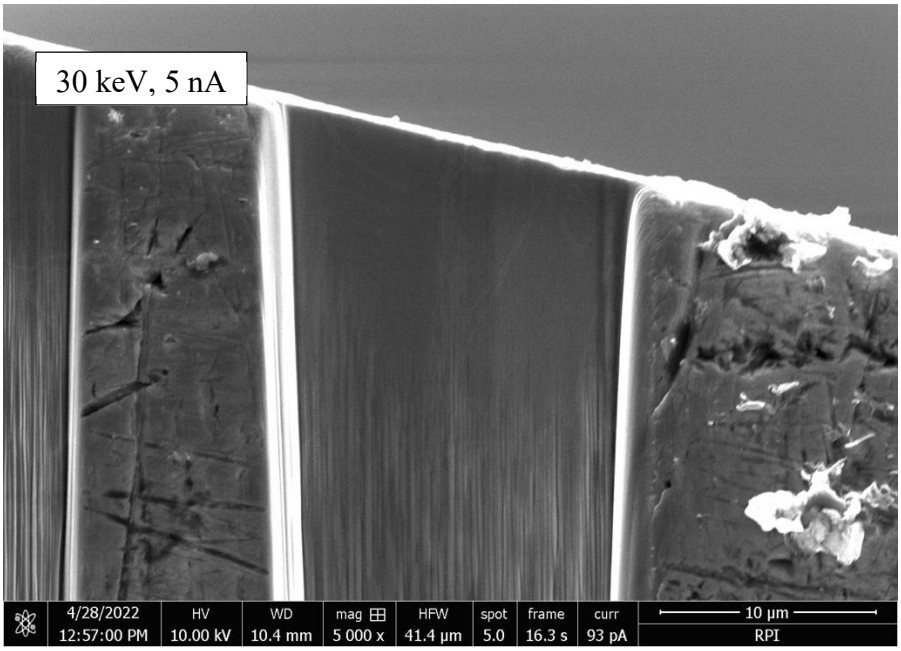
30 keV, 5 nA
4/28/2022
12:57:00 PM
HV
10.00 kV
WD
10.4 mm
mag
5 000 x
HFW
41.4 µm
spot
5.0
frame
16.3 s
curr
93 pA
10 µm
RPI

Appendix C Additional EBSD Images

C.1 FIB current effects on EBSD Overview